

Available online at www.sciencedirect.com

jmr&t
Journal of Materials Research and Technology
journal homepage: www.elsevier.com/locate/jmrt



Original Article

A study on a hybrid SERS substrates based on arrayed gold nanoparticle/graphene/copper cone cavities fabricated by a conical tip indentation



Jingran Zhang ^{a,b}, Siwei Lu ^{a,b}, Guangfeng Shi ^b, Wenkun Xie ^c,
Yanquan Geng ^{d,*}, Zuobin Wang ^a

^a Ministry of Education Key Laboratory for Cross-Scale Micro and Nano Manufacturing, Changchun University of Science and Technology, Changchun 130022, PR China

^b Department of Mechanical and Electric Engineering, Changchun University of Science and Technology, Changchun 130022, PR China

^c Centre for Precision Manufacturing, DMEM, University of Strathclyde, Glasgow, G1 1XJ, UK

^d Center for Precision Engineering, Harbin Institute of Technology, Harbin, Heilongjiang 150001, PR China

ARTICLE INFO

Article history:

Received 20 September 2022

Accepted 1 December 2022

Available online 5 December 2022

Keywords:

Tip-based indentation

SERS

Graphene

Malachite green

Paraquat

ABSTRACT

The pesticide residues with low concentration are important to detect in food safety. Although a lot of methods, such as spectrophotometry, colorimetry and liquid chromatography, are used to detect pesticide residues, they often suffer from low efficiency and long detection time. Here, a hybrid Surface Enhanced Raman Scattering (SERS) substrate, namely, Au nanoparticle/copper-based graphene/arrayed cone cavities (Au@GR@Cu cone cavities), is fabricated for pesticide residues detection through sputtering Au nanoparticle and generating periodical cone cavity structures on the copper-based graphene surface. By actively controlling the interspace between adjacent cone cavities, both surface topographies and the number of graphene layers on the SERS substrate could be modulated, creating an effective control on the functional performance of the SERS substrate. Both sensitivity and reliability of the hybrid SERS substrate were evaluated by Raman Spectroscopy detection. The experimental results indicated that both 10^{-9} mol/L malachite green and 10^{-7} mol/L paraquat could be detected, respectively. Moreover, the detected Raman intensity of malachite green only dropped by 11.89% in a month and 29.8% in two months, respectively. The hotspot distribution was also characterized by 2-dimensional Raman mapping. The research finding is expected to provide a new insight in development of innovative SERS substrates.

© 2022 The Author(s). Published by Elsevier B.V. This is an open access article under the CC BY-NC-ND license (<http://creativecommons.org/licenses/by-nc-nd/4.0/>).

* Corresponding author.

E-mail address: gengyanquan@hit.edu.cn (Y. Geng).

<https://doi.org/10.1016/j.jmrt.2022.12.001>

2238-7854/© 2022 The Author(s). Published by Elsevier B.V. This is an open access article under the CC BY-NC-ND license (<http://creativecommons.org/licenses/by-nc-nd/4.0/>).

1. Introduction

Low-concentration detection of Malachite green (MG) and Paraquat (PQ) is of great importance to ensure food safety and human healthy. MG is widely employed in aquaculture, especially fishery due to its low price and good bactericidal effect [1]. MG is a Class II health hazard with thermally stability and may not fully degrade in conventional fish processing [2], which potentially threat the human health [3]. The concentration of MG cannot exceed 5.727×10^{-9} mol/L in the National Food Safety standard of China (GB 2763.1-2018). The minimum required performance limit of MG approved by the European Commission is 2 $\mu\text{g}/\text{kg}$ [4] whereas MG is banned for any aquatic species in U.S [5]. PQ is a herbicide for agricultural weed growth, but it may induce cell damage and necrosis in the heart, liver and kidney of human [6]. The maximum residue limit for PQ in food in the U.S. is 0.01–1 mg/kg [7,8]. Currently, various methods have been applied to detect MG or PQ, such as spectrophotometry [9], liquid chromatography [10], gas chromatography [11] and colorimetry [12]. For instance, Abbas Afkhami et al. [9] extracted and desorbed MG combining nanoparticle adsorption and magnetic separation, and realized the detection of the MG at a concentration of 0.28 ng/mL using the spectrophotometry method. Gao et al. [10] fabricated melamine sponge using β -cyclodextrin and graphene oxide as an extraction adsorbent, which was coupled with liquid chromatography method to achieve the detection of MG molecules at a concentration of 0.21 mg/L. Headspace solid phase microextraction was employed to determine the PQ of urine and the limit of detection was 0.1 ng/mL by gas chromatography method [11]. Jia et al. [12] used a colorimetric aptasensor based on unmodified Au nanoparticles for selectively detection of MG with a detection limit of 15.95 nmol/L.

Overall, although current available methods can be applied to accomplish the detection of pesticide residues, they are time consuming and usually require complex pre-treatment procedures, capital intensive instruments and well-trained technicians. Therefore, developing innovative, simple, fast and low-cost detection method is of great significance for meeting rapidly-developed demand for low concentration detection of pesticide residues.

SERS technology has found wide applications in high accuracy detection of pesticide residues [13,14], pigment additives in food, explosives and pathogens in the environment. At present, scholars generally believe that the mechanism of SERS enhancement includes the electromagnetic enhancement (EM) [15] and the chemical enhancement (CM) [16]. EM caused by local surface plasmon resonance (LSPR) is the mainly factor of the SERS enhancement. CM is related to the charge transfer between the adsorbed molecule and the SERS substrate, improving the resolution of the signal.

Especially, three-dimensional periodical functional micro/nanostructures were found to effectively modulate the performance of SERS substrates through changing structural shape, size and distribution. However, the wide application of SERS techniques is still limited by challenges in substrate fabrication, including structural homogeneity, stability,

complexity and low cost. In this context, various fabrication methods were utilized for generating micro/nanostructures as SERS substrates. He et al. [17] combined arrayed Si nanopillar fabricated by photolithography and deep-Si etching, sputtered Au nanoparticles and assembled Ag nanoplates, achieving the detection of 10^{-12} mol/L 3-nitro-1,2,4-triazol-5-one. Kundan Sivashanmuga et al. [18] fabricated a SERS substrate by using FIB technology to produce arrayed hemispherical ZnO dome structures on a Si plate, and electron beam deposition to deposit Ag nanoclusters. It can realize the detection of MG at a concentration of 10^{-17} mol/L. A porous Si/Au SERS substrate with an enhancement factor (EF) of 10^{11} were formed on the Al/Si alloy surface by combining laser-induced periodical structure generation and sputtering methods [19]. By combining electrodeposition and self-assembly methods, Wang et al. [20] generated the Au/Ag alloy microstructures on arrayed Si pillar as SERS substrates that are capable of detecting 10^{-12} mol/L R6G.

Dong et al. [21] fabricated an Au-coated TiO_2 macroporous as SERS substrates. The best SERS performance is generated that the pore size of the porous structure is 290 nm and the thickness of the gold film is 80 nm. The prepared porous substrate can capture exosomes in the plasma. Zhang et al. [22] fabricated hollow nanocones at the bottom of microbowls to form volume enhanced Raman scattering substrates (VERS) and the adenovirus type 5 was detected by using the VERS substrates. Due to the controllability of the nanocone size, the substrate can capture a single virus and complete the work of collecting a comprehensive Raman signal of a single virus. Giovanna Palermo et al. [23] fabricated a gold-plated inverted pyramid-shaped nanopore SERS substrate on a glass substrate by combining EBL lithography and electron beam evaporation method and the hepatitis A virus with a concentration of 13 pg/mL was detected. Durmanov et al. [24] fabricated size-controlled porous SERS substrates of silver nanofilms with rough surfaces by electron beam vapor deposition. The four virus are identified by using the SERS substrates. The Au covered polymer arrayed nanostructures are machined by combining roll-to-roll ultraviolet and nanoimprint lithography methods and the highest enhancement factor is 1.21×10^7 [25].

The addition of graphene in SERS substrates can not only increase the adsorption amount, but also decrease the background fluorescence of detection probe molecules, thereby effectively improving the molecule sensitivity of detection probe [26,27]. Zhao et al. [28] produced a hybrid structure of arrayed AuNPs/graphene/hexagon Ag nanoholes by combining electron beam lithography (EBL), magnetic sputtering with chemical vapor deposition (CVD) methods, and the crystal violet was detected at a concentration of 10^{-12} mol/L. The arrayed graphene/Au nanopyramids with an enhancement factor of 10^9 for R6G and methylene blue could be fabricated by combing colloidal lithography, O_2 plasma etching, magnetron sputtering with CVD methods [29]. Zhao et al. [30] fabricated arrayed graphene vertical gold nanorods as SERS structures using self-assembly and wet-etching methods. In addition, the 10^{-9} mol/L R6G and CV were detected, respectively.

In our previous study, the enhancement effect of graphene on the detection sensitivity was also demonstrated [31]. However, the influence of surface topography and the number

of graphene layers on Raman spectrum intensity of target molecules are not known, which has become one important knowledge gap for the design and development of innovative and optimal hybrid SERS substrate of Au nanoparticle copper-based graphene arrayed cone cavities.

For this reason, in our study, a hybrid SERS substrate of Au nanoparticle/copper-based graphene/arrayed cone cavities was first fabricated through sputtering Au nanoparticle and fabricating periodical cone cavity structures on copper-based graphene surface. On this basis, both the surface topographies and the number of graphene layers onto the SERS substrate were analyzed. And MG were employed as a target molecule for SERS performance evaluation. In addition, the characteristic peak of PQ residues on the SERS substrate was identified. Finally, the electromagnetic enhancement mechanism of hybrid SERS substrate was studied.

2. Materials and methods

Copper-based graphene template was purchased from Nanjing Jicang Nano Technology Co., Ltd. Malachite Green (MG, 99% purity) dye and Paraquat (PQ, 99% purity) were purchased from Aladdin. All the samples were cleaned in ethanol.

The home-built normal force control system established in our previous works was used to fabricate micro/nano-structures [32–35]. Fig. 1 showed the schematics of the fabrication and performance evaluation process of the hybrid SERS substrate. The arrayed cone cavities on the copper-based graphene surface were first generated by a conical tip-based indentation method, in which the interspace of the adjacent cavities in the X and Y direction could be changed by varying the machining feed. Then, a 10 nm gold film was coated on the copper-based graphene surface by magnetron sputtering to avoid the influence of oxidation and enhance the plasmon effect. Finally, the probe molecule solution at a concentration of 1 mL was dropped on hybrid substrate. After the solvent

ethanol was evaporated, Raman spectra detection was subsequently conducted.

The surface morphologies of the SERS substrate were detected by a scanning electron microscope (SEM, Zeiss). Atomic force microscopy (AFM, Dimension Icon, Bruker) was employed to detect the 2D and 3D surface topographies. The UV–Vis adsorption spectra were employed in the range of 200–800 nm using a UV-3600 spectrophotometer. Raman spectra on the sample were recorded using a Renishaw InVia Raman spectrometer and a confocal microscope employing a diode laser operating at 633 nm. A $50\times$, 0.75 NA Leica objective was employed to focus the laser light on the samples.

3. Results and discussion

3.1. Characterization of the arrayed micro/nano cone cavities

As described above, the interspace between adjacent cone cavities in the X and Y directions was changed to produce different surface topography, which ranged from $1\ \mu\text{m}$ to $10\ \mu\text{m}$ in an area of $30\times 30\ \mu\text{m}^2$. Table 1 summarized the surface morphologies and typical structural features of the fabricated substrates, which were referred to Cone 1–Cone 9, respectively. Fig. S1 showed the SEM images of samples after sputtering gold film (a) Cone 1, (b) Cone 5, (c) Cone 6, (d) Cone 8, (e) Cone 9.

Fig. 2 showed the surface topographies of different pre-designed interspace of cone cavities. On cone 1, paraboloid-shaped cone cavities were formed at a large interspace of $10\ \mu\text{m}$, as illustrated in Fig. 2 (a). The typical surface topography features of the cone 1 were cavity structure, except for the large original flat area of substrate. As the interspace decreases in both x- and y-directions, the adjacent cone cavities were gradually overlapped, which not only changes the surface topography, but also varies the SERS performance.

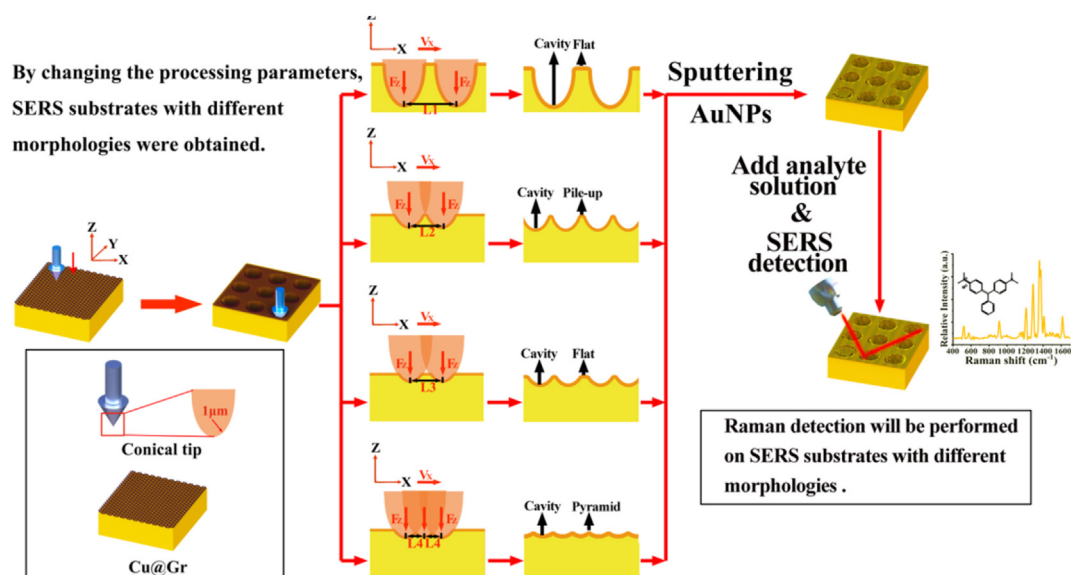
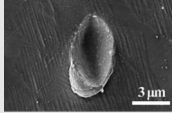
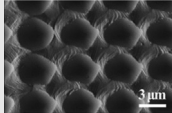
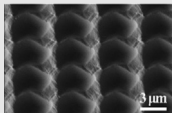
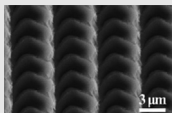
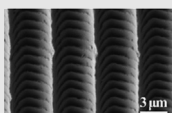
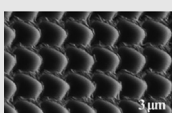
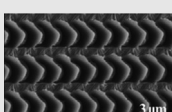


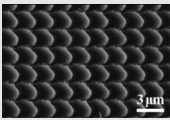
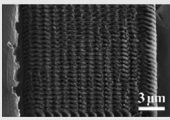
Fig. 1 – Schematic diagram of fabrication of the hybrid substrate.

Table 1 – The cone cavities with different X and Y direction interspaces.

Abbreviated Name	X-direction interspace (μm)	Y-direction interspace (μm)	SEM image	Typical structural features
Cone 1	10	10		Single Cavity
Cone 2	5	4		Cavity & Flat
Cone 3	5	3		Cavity & Flat
Cone 4	5	2		Cavity & Pile-up
Cone 5	5	1		Cavity & Pile-up
Cone 6	3	3		Cavity & Flat
Cone 7	2	4		Cavity & Pile-up

(continued on next page)

Table 1 – (continued)

Abbreviated Name	X-direction interspace (μm)	Y-direction interspace (μm)	SEM image	Typical structural features
Cone 8	2	2		Cavity & Pyramid
Cone 9	2	1		Cavity & Pyramid

On the Cone 2, Cone 3 and Cone 6, due to the decreased interspace, the flat area between cavities also plays essential role in enhancing the electrochemical properties of the SERS substrate. In this case, the shrunk flat area could serve as one kind of functional structure on the substrate surface, which is different from the large flat area on the Cone 1. Besides, on the Cone 4, Cone 5 and Cone 7, at the x-direction interspace of $5\ \mu\text{m}$ and y-direction interspace of $1\text{--}2\ \mu\text{m}$, the fabrication-induced pile-up structures will replace the flat area as the dominating topographical structure. Especially, at the interspace of $1\ \mu\text{m}$, evident ribbon structures are generated on the substrate surface (see Fig. 2(b)). Moreover, on the Cone 8 and Cone 9, the pyramid structures became a part of the cone cavities with good consistency, as illustrated in Fig. 2(d). Overall, as the interspace changes, the typical structural feature of the SERS substrate undertakes an evident transformation across cavity, flat area, pile-up and pyramid structures, effectively modulating the performance of SERS substrate, which will be discussed in-detail in the subsequent sections.

The peak-to-valley height of copper-based graphene cone cavities were further characterized, as shown in Fig. 3. As the interspace of adjacent cone cavities decreases in either x- or y-direction, both peak-to-valley height and area of cone cavities decrease, while the cone density increases. On Cone 1, the peak-to-valley height of cone cavities was $2.3\ \mu\text{m}$ and there were 9 cone cavities generated in an area of $30 \times 30\ \mu\text{m}^2$. Differently, the peak-to-valley heights of cone cavities on Cone 9 was only approximately $150\ \text{nm}$, and 450 cone micro-cavities are formed in an area of $30 \times 30\ \mu\text{m}^2$. The surface roughness tends to increase with the decreased interspace distance (Table S1), which should be ascribed to the increase in the density of cone cavity, pile-up and pyramid structure formed on the surfaces. Overall, both morphology and roughness of the substrate surfaces are influenced by the interspace of the cavities.

3.2. Analysis on the number of graphene layers

In the tip-based indentation process, the distribution of graphene on the substrate surface is inevitably changed. It is

critically important to investigate the fabrication-induced variation of the number of graphene layers on the processed surface, which contributes to fully understand the underlying mechanism of how the number of graphene layers affects the Raman signal distribution of the substrate surface. Since it is hard to directly identify graphene layers by SEM on the new substrate surface, thus a conventional Raman measurement was carried out. The Raman spectra of graphene with 3 random positions were measured on the pile-up region and cavity region of Cone 5, respectively. The Raman spectra hybrid substrate surface and the corresponding AFM images are shown in Fig. 4(a). The D, G, and 2D characteristic peaks of graphene were detected at 1360 , 1580 , and $2695\ \text{cm}^{-1}$, which indicates the presence of graphene on the pile-ups and cone cavities, as shown in Fig. 4(a). The D band related with defects in graphene originates from the breathing mode of sp^2 hexagonal carbons. The D peak should be attributed to the overlapped cone cavities. The peak intensity ratio (I_G/I_{2D}) of the Raman spectra could be used to identify the number of graphene layers [36,37]. Fig. 4(b) compares the Raman spectra of graphene of different substrate surface, namely, Cone 1, Cone 2, Cone 3, Cone 5, and Cone 7, as well as the original flat surface. On the flat surface, Cone 1 (single cavity), Cone 2 (cavities & flat) and Cone 3 (cavities & flat), the intensity ratio of I_G/I_{2D} is less than 0.7, which means the existence of monolayer graphene on Cu surface. Differently, on the Cone 5 (cavities & pile-up), Cone 7 (cavities & pile-up), Cone 8 (Cavity & Pyramid) and Cone 9 (Cavity & Pyramid), the value of I_G/I_{2D} ranges from 0.7 to 1.3, which represents the typical features of bilayer graphene, as shown in Fig. 4(b). Therefore, above research results indicate that the number of graphene layers was actually affected by different topographies.

3.3. Performance evaluation of the hybrid SERS substrate

The three position of composite SERS substrate is chosen by using Ultraviolet visible spectrophotometer. The absorption spectrum curves basically coincide on the three position. The absorption peaks at $320\ \text{cm}^{-1}$ and $490\ \text{cm}^{-1}$, and the peak

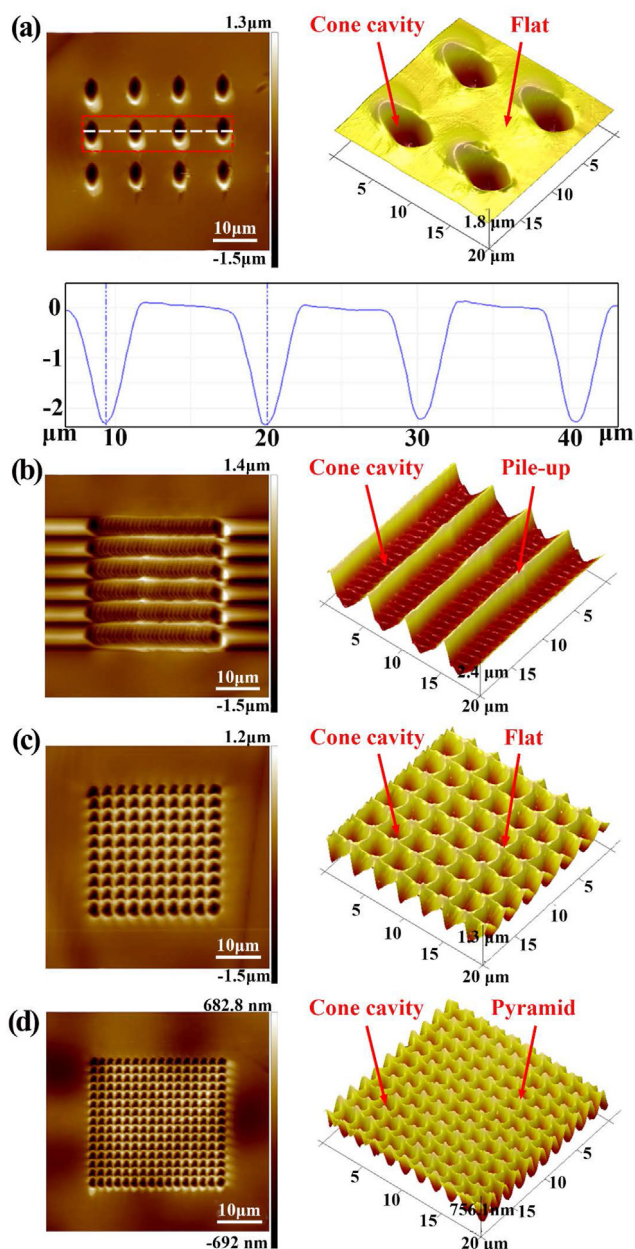


Fig. 2 – AFM images of two-dimension, three-dimension and corresponding cross-sectional profile (a) Cone 1. (b) Cone 5. (c) Cone 6. (d) Cone 8.

width becomes wider, as shown in Fig. S2. The decrease of the absorption peak intensity and the broadening of the spectra are resulted from a contribution of numerous smaller different sizes surface features. The broadening of the plasmon resonance is owing to the nanoparticles aggregation, resulting in stronger dipole–dipole interactions.

In order to estimate the SERS performance of the hybrid substrates, Fig. 5(a) showed the characteristic peaks of 10^{-8} mol/L MG on different substrates. All the characteristic peaks of MG were identified by different hybrid substrate and matched well with results reported in the literature [38,39]. In the present work, the SERS peak at 1362 cm^{-1} represented the average

Raman intensity of MG on the substrate surface. Fig. 5(b) summarized the intensities of the SERS peak at 1362 cm^{-1} on different substrate surfaces. Compare with the Cone 1 (single cavities), the Raman intensities of Cone 2, Cone 3 and Cone 4 (cavities & flat) were slightly increased, indicating that the density of cavities increased and the hot spots improved. The Raman intensities of Cone 5 and Cone 7 (cavities & pile-up) were larger than that of Cone 2, Cone 3 and Cone 4 (Cavities & flat). The Cone 8 and Cone 9 (Cavities & pyramid) showed the highest Raman intensity with a well-controlled derivation range of smaller than 7%, indicating that the substrates exhibit the highest SERS sensitivity and good stability. This phenomenon was primarily due to the difference in cone cavity size, spacing and density, which directly affects the hot spots distribution on the SERS substrate. Compared with the other structures, more pile-ups or pyramids were generated on the modified substrates surfaces, which also represents that more hot spots were formed substrate surface, thereby enhancing the Raman intensity of MG molecules.

Fig. 5(c) and (d) summarized the Raman intensity of 8 randomly measured positions on the pyramid region of the Cone 8 and Cone 9 substrates, respectively. The relative standard deviation (RSD) values of the peaks at 1292 cm^{-1} and 1362 cm^{-1} on Cone 9 were 6.34% and 6.35%. While those on Cone 8 were 6.98% and 7.44%, respectively. The low RSD values deviation (below 10%) of the peaks at 1292 cm^{-1} and 1362 cm^{-1} peaks on substrate surfaces indicates the high homogeneity of surface topographies and number of graphene layers.

The signal stability of the SERS substrate was also critically important in practical applications. In this work, the SERS substrates were also evaluated through Raman spectroscopy detection of 10^{-8} mol/L MG after storage in air for 1 day, 1 month, and 2 months. As shown in Fig. 5 (e) and (f), the detected Raman intensities of MG on the Cone 8 and Cone 9 after 1 month, were 94.34% and 88.11% of the initial value (1 day), while those were 69.8% and 70.2% of the initial value (1 day) after two months.

Overall, above Raman spectroscopy detection experiments indicated high sensitivity, uniformity and stability of the proposed hybrid SERS substrate.

Additionally, it is crucial to understand the underlying mechanism of how the structural features on the hybrid substrates affect SERS signal. Fig. 6(a)–(d) showed the results of Raman mapping images of 10^{-8} mol/L MG on different substrate surfaces. On Cone 1 and Cone 6, cone cavity exhibited an evidently-enhanced Raman signal intensity, compared with the flat surface, as indicated by the arrows in Fig. 6(a) and (c). On Cone 5 and Cone 8, the maximum Raman intensities of MG were 1400 and 2500 (see Fig. 6(b) and (d)), which were much larger than those on Cone 1 and Cone 6. Such a large difference is due to the pile-up and pyramid structures. Thus, it can be inferred that pile-up and pyramid structures have a larger enhancement effect on Raman spectrum intensity than cone cavity, contributing to increasing the SERS activity of the SERS substrate.

The Raman intensity at 1292 cm^{-1} on pile-up region of Cone 5 was about 3 times larger than that on cavity in Fig. 6(e) and (f). The Cone 6 cavity region showed a stronger Raman intensity at 1292 cm^{-1} , which was 1.8 times larger than that on

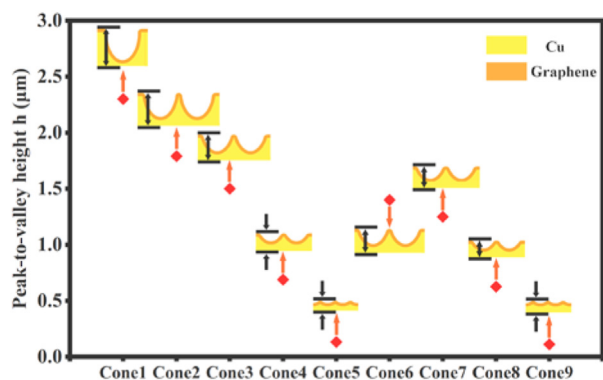


Fig. 3 – Heights of peak-to-valley of cone cavities with different topographies and the sectional views of corresponding cone cavities.

the flat region (Fig. 6(g) and h). On Cone 8 surface, the Raman intensity at 1292 cm^{-1} of pyramid region was about 2.5 times larger than that of the cavity region (Fig. 6(i) and j). It can be inferred that the enhancement effect of different structural feature on Raman intensity follows the order of pyramid \geq pile-up $>$ Cavity $>$ flat area, which provide new inspiring insights to create accurate control on the activity of the SERS substrates. In addition, all points from the same region produced almost identical Raman signals under the same experimental

conditions, demonstrating the good reproducibility for the hybrid substrates for low concentrations of the probe molecule.

The concentrations of MG solution can not exceed $5.727 \times 10^{-9}\text{ mol/L}$ in the Food Safety standards of Chinese National. Using the hybrid substrate, the detection limits for MG was 10^{-9} mol/L (Fig. S3), proving the applicability of the substrate for food safety.

To demonstrate detection capability of the hybrid substrates for diverse molecules, the Raman spectra of PQ at the concentration of 10^{-7} mol/L was also measured, as shown in Fig. 7(a). Obviously, the Cone 8 and Cone 9 exhibit a highest Raman spectra intensity and the RSDs were smaller than 8%, as shown in Fig. 7(b). The RSDs of the Raman peaks of Cone 9 at 652 cm^{-1} and 1294 cm^{-1} were 6.55% and 6.73%, respectively, as shown in Fig. 7(c). Moreover, the Raman intensity of Cone 9 only decreased by 19% and 27% after the storage for 1 month and 2 months, respectively. The Raman signal intensity of Cone 8 only decreased by 19% and 35% after 1 month and 2 months, respectively, exhibiting an extremely stable SERS performance.

3.4. Study on the electromagnetic enhancement mechanism of SERS substrate

The local electric field characteristics of the arrayed hybrid substrates were calculated by the COMSOL software. Figs. S4

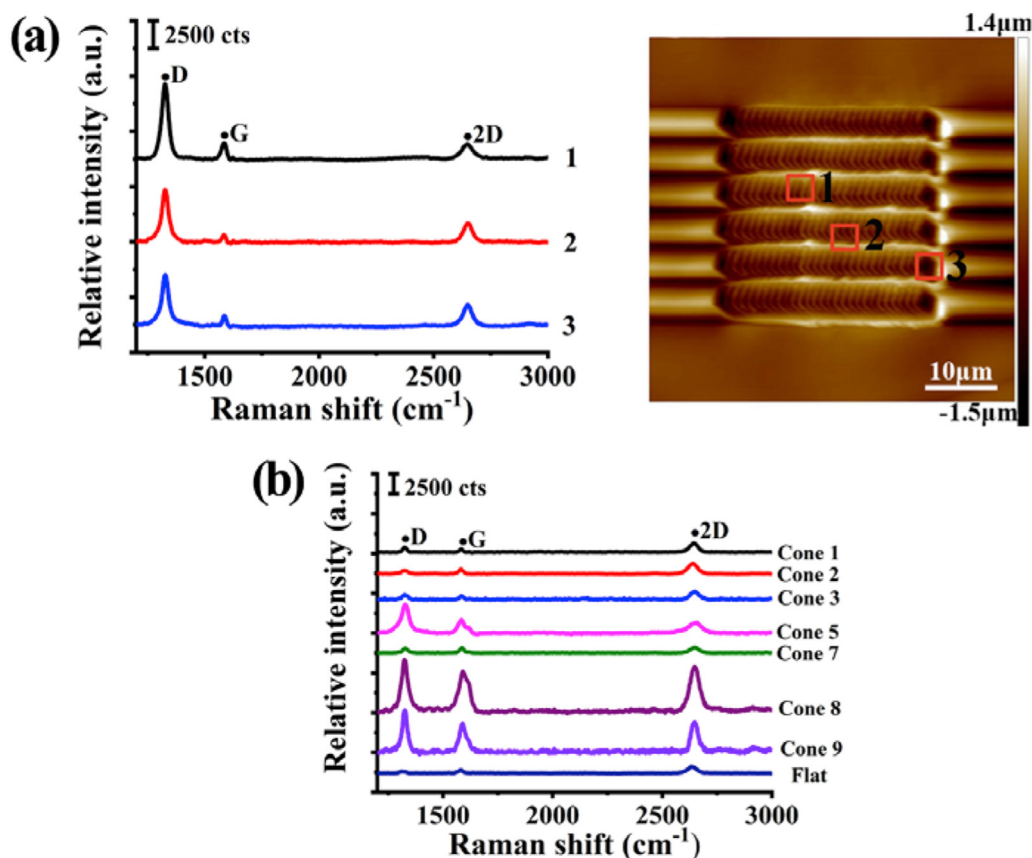


Fig. 4 – Raman spectra detection results of graphene (a) different regions on Cone 5 and corresponding AFM image. (b) Cone cavity region on different substrates.

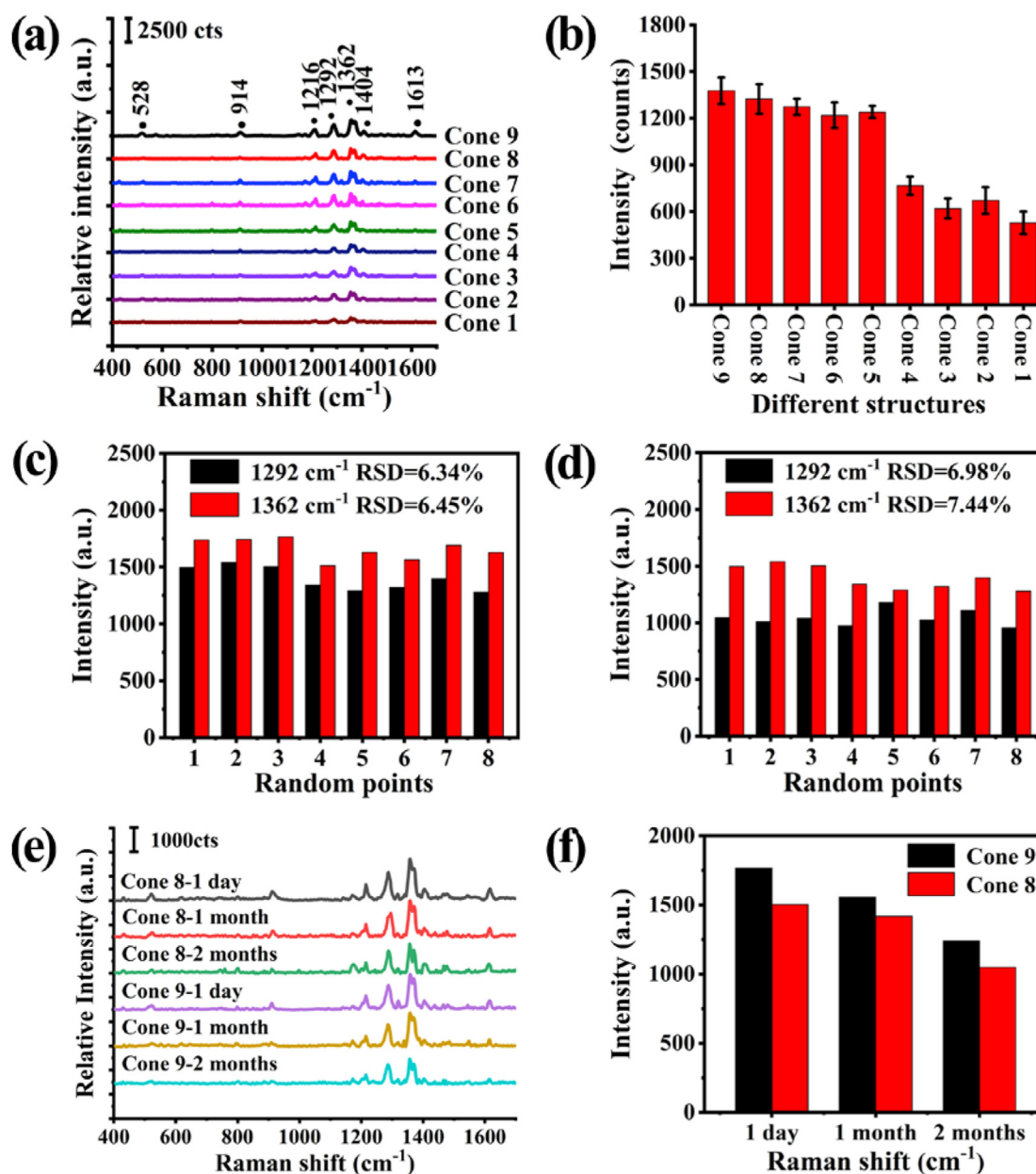


Fig. 5 – (a) Raman spectra of 10^{-8} mol/L MG on the different substrates. (b) Average Raman intensity of peak at 1362 cm^{-1} on different substrates. Raman intensity distributions of MG at 1292 cm^{-1} and 1362 cm^{-1} on Cone 9 (c) and Cone 8 (d). (e) Raman spectra of 10^{-8} mol/L MG and (f) Raman intensity of MG at 1362 cm^{-1} on the Cone 8 and Cone 9 after 1 day, 1 month, and 2 months, respectively.

and 8 compare the calculated local electric field of different hybrid SERS substrates in the X–Z plane to clearly illustrate the influence of single cone cavity and pyramid structures. The incident wavelength, the thickness of graphene and diameter of Au NPs were set to 633 nm, 0.34 nm, and 80 nm [31,40], respectively. The scale was logarithm $|E/E_0|$. Figs. S4(a) and S4(b) showed the electrical field distributions of Cone 1 and Cone 8, respectively. The electric field intensity of Cone 8 was 19.35 V/m, which was 4 times than that of Cone 1. With the decrease of interspace, a stronger electrical field was generated on the pyramid of adjacent cone cavities (Fig. S4(b)). Thus, effective plasma coupling could be achieved between

adjacent cone cavities on the copper-based graphene surfaces by controlling interspace, which can further improve the SERS performance substrate.

Two enhanced electric field regions (hot spot) are formed at the gaps between nanoparticles and copper-based graphene surface, while a hot spot with the maximum electric field intensity of 768.672 V/m is formed at the gap of nanoparticles on the Cu-based graphene surface, as shown in Figs. S4(c) and 8(a). Due to the influence of surface topography, the electric field distribution on the substrate surface is substantially changed. As shown in Fig. 8(b), when the substrate surface is modified with the single cone cavity structure, the electric

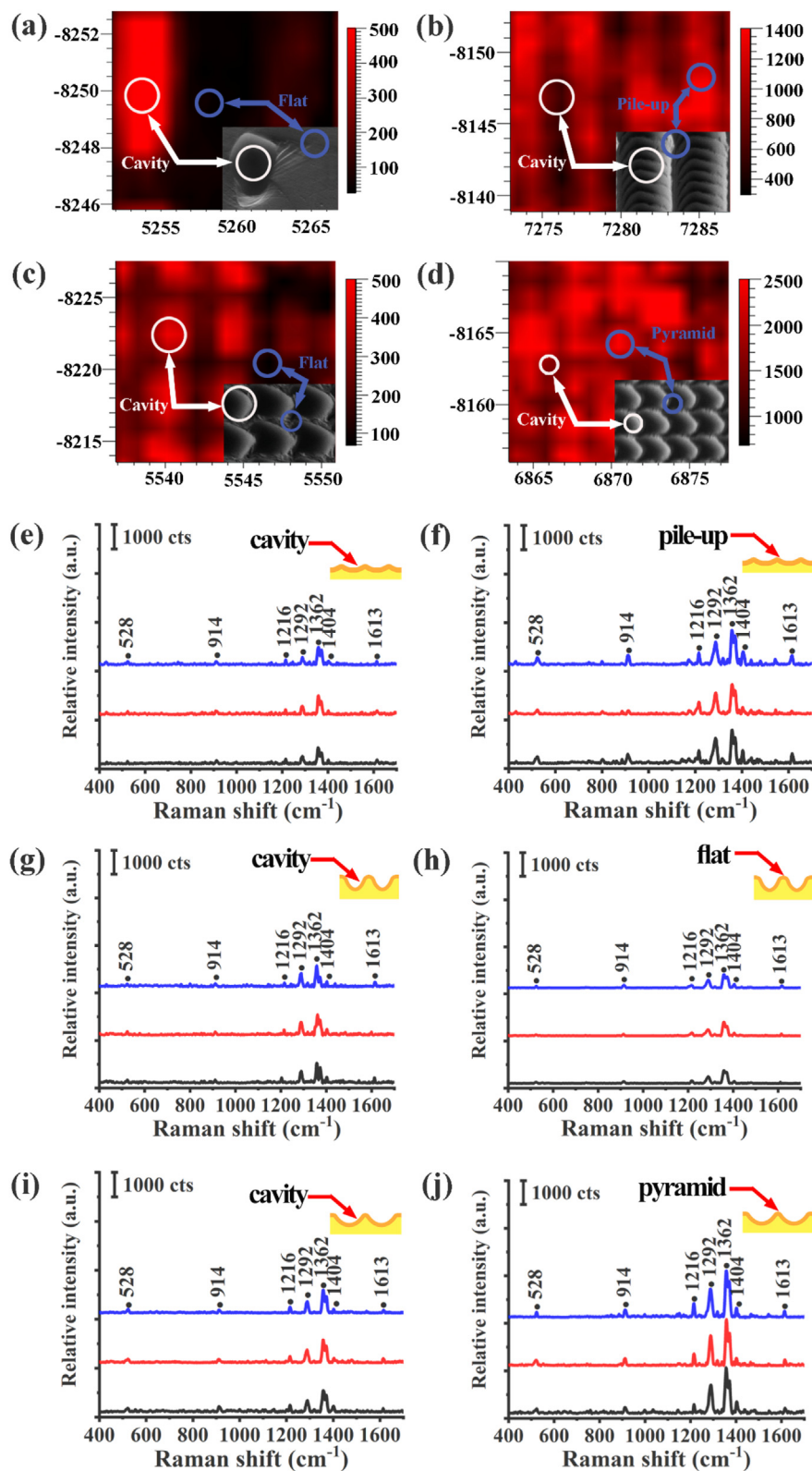


Fig. 6 – Raman mapping images of 10^{-8} mol/L MG on different substrates. (a) Cone 1, (b) Cone 5, (c) Cone 6, (d) Cone 8. The Raman spectra of MG on cone cavity (e) and pile-ups (f) of the Cone 5, cone cavity (g) and flat area (h) of the Cone 6, cone cavity (i) and pyramid (j) of the Cone 8.

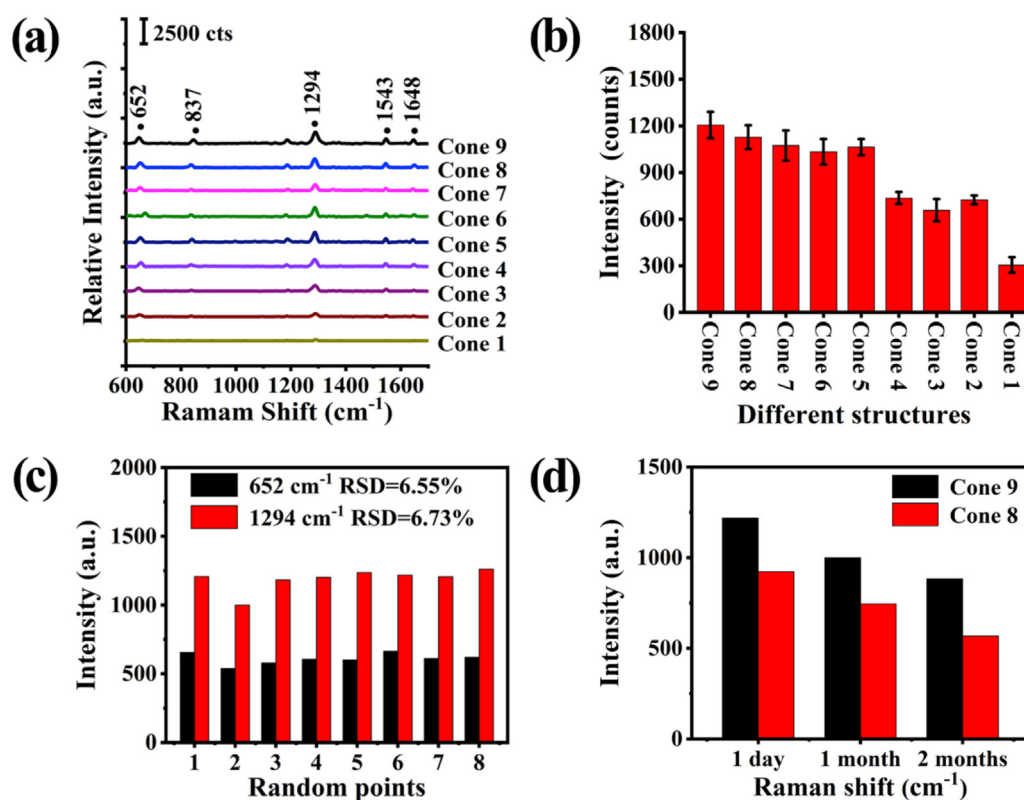


Fig. 7 – (a) Raman spectra of 10^{-7} mol/L PQ on different substrates. (b) Average Raman intensity of PQ at 1294 cm^{-1} for different substrates. (c) Raman intensity of PQ at 652 cm^{-1} and 1294 cm^{-1} on pile-up region of Cone 9. (d) Raman signal of PQ at 1294 cm^{-1} on the Cone 9 and Cone 8 after 1 day, 1 month, and 2 months, respectively.

field strength at the gap of Au nanoparticles is up to >2600 V/m, and the enhancement factor is over 3.4 times larger than conventional surface. The intensively localized and enhanced electric field are initiated by resonance coupling at the gaps of adjacent Au NPs and those gaps of Au NPs above cone cavity.

Compared with the gaps of nanoparticles on the conventional Cu-based graphene surfaces, due to the generation of the single cone cavity, a small volume is formed between nanoparticles and cone cavity. In Raman spectrum detection, when incident light is irradiated on SERS substrate, the incident light would be reflected inside the small volume with many times, and is finally absorbed by nanoparticles, thereby improving the Raman intensity in the detection area. Consequently, more hot spots are formed at the gaps of Au nanoparticles within the single cone cavity within same area.

As shown in Figs. S4(e) and 8(c), on the pyramid structure-modified substrate surface (Cone 8), the maximum electric field intensity at the gap of Au nanoparticles is 10,646 V/m, exhibiting an enhancement factor of 4 times larger than single cone cavity-modified substrate surface. Additionally, due to the pyramid formed by the overlapped cone cavities, the Au nanoparticle on the Cone 8 show an increased hot spot distribution than that on Cone 1. The maximum enhanced electric field lies between Au NPs in the pyramid structure, as shown in Fig. 8(c). As shown in Figs. S4(f) and 8(d), on the pyramid structure-modified substrate surface (Cone 9), the maximum electric field intensity at the gap of Au nanoparticles is 17,250 V/m, exhibiting an enhancement factor of 6.6 times larger than single cone cavity-modified substrate

surface, respectively. The local electric field enhancement can be effectively excited between two adjacent Au NPs, and also formed between the Au NPs above pyramid.

Intensive localized electric field enhancements initiated by resonance coupling are concentrated between two adjacent Au NPs, and also formed between the Au NPs above pyramid. Compared with the nanoparticles on the single cone cavity, a pyramid structure is formed (see Fig. 8(c)), the tip of the pyramid structures causes a larger plasma resonance, enhancing the electric field intensity. Then, due to the change of topological structure, new small volumes are formed between nanoparticles, pyramids and graphene. The light can be focused to a very small volume, resulting in a huge near-field enhancement effect. Compared with the cavity structure shown in Fig. 8 (b), the number of small volumes per unit area increases. The structure and volume of cavity have a significant effect on the intensity of electric field so as to improve its Raman strength.

As discussed above, the EM tightly correlates with the spacing of adjacent graphene/Cu cone cavities and the Au NPs on the structured substrate, which can amplify electrical field intensity of the plasmonic resonance.

4. Discussion

The enhanced Raman detection capability of the proposed hybrid substrate can be assigned to the following reasons: (1) different surface topographies at different pre-designed

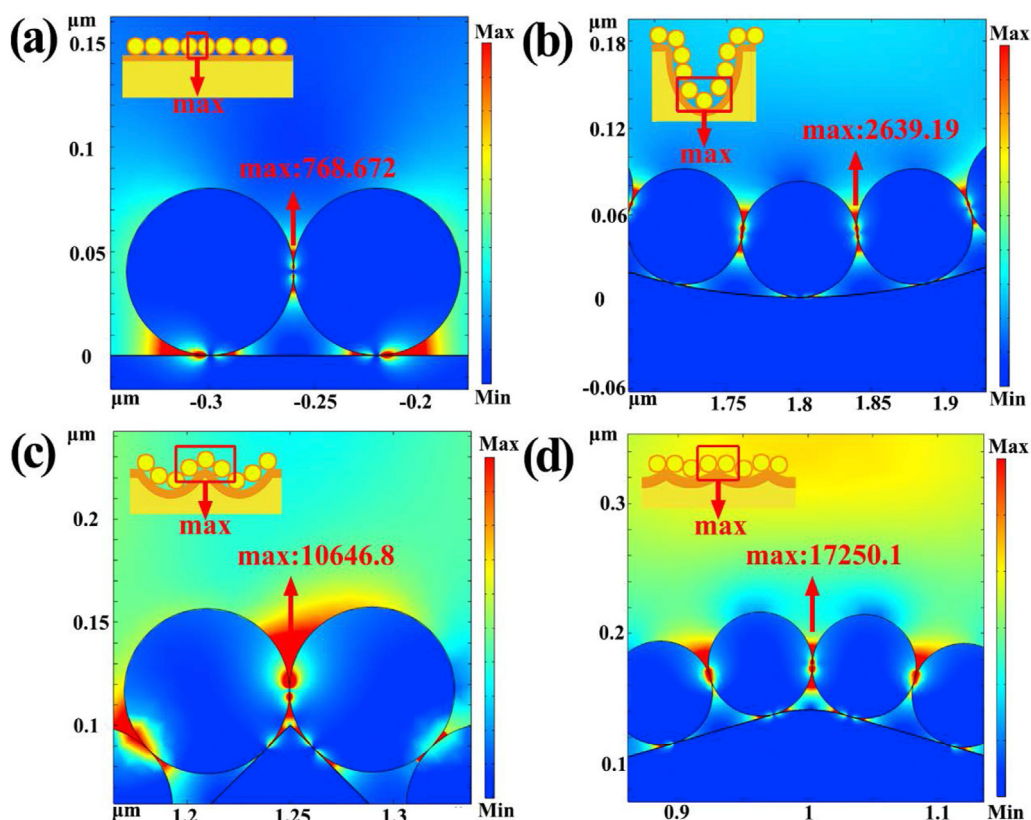


Fig. 8 – Simulations of the electric field distributions of adjacent nanoparticles on the graphene/Cu surface (a), Cone 1 (b), Cone 8 (c), Cone 9 (d).

interspaces, (2) electric field distribution, (3) High surface roughness, (4) the chemical enhancement effect brought by different layer numbers of graphene.

The Raman intensity tends to gradually increase with the decrease of interspaces. This phenomenon is primary due to the different in cone cavities size and density at different interspaces of cone cavities on the hybrid substrates, resulting in the difference hot spot distribution on the SERS substrate, as shown in Fig. 9. In addition, the pyramid and pile-ups were generated with the decrease of interspaces, resulting in LSPR. The surface roughness was increased and the more hot spots were generated on the pile-up region (Fig. 9(b)), resulting in the increasing of Raman intensity. The Raman intensity was highest on the tip of pyramidal structures due to the larger LSPR generated on the tip region of pyramidal structures [41]. The more cone cavities & pyramid structures (Fig. 9(d)) can

enhance the Raman intensity of target molecules. The coupling effect of the cone cavities and Au nanoparticles contribute to enhancing the local electromagnetic field further. Then, Au NPs on the graphene/Cu cavities generated new nanogaps and increased the density of hot spots, thus enhancing electric field intensity. In addition, the warped spaces can generate an effective refractive index gradient [42], mitigating the change in the refractive index from air to the gold nanoparticle/graphene/Copper cone cavities surface.

Benefiting from the large specific surface area of the 3D pyramidal structure, the hot spots are resonantly excited by the adsorbed AuNPs, thereby contributing to the improvement of the SERS performance. Hot spots can be formed in experimentally fabricated cone cavities because Au NPs and graphene can assist with uniform nanogap formation. The more Au NPs are aggregated on the same area, the easier it is

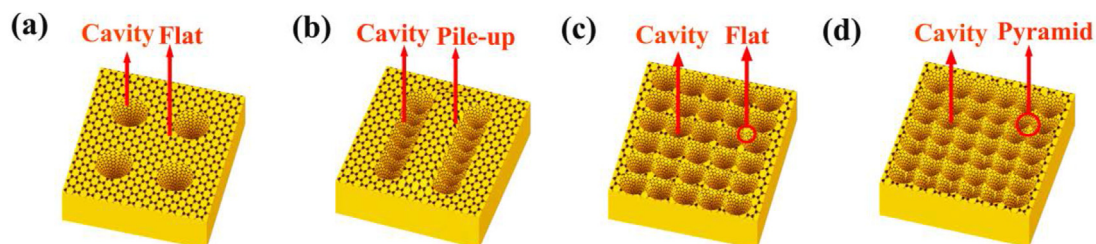


Fig. 9 – Schematic diagram of different cone cavities topographies fabricated by a conical tip.

for resonance coupling to occur, providing stronger hot-spots for SERS. On the hybrid substrate, the Au plasmons will be excited by the irradiation of the incident light. For the co-existence of the resonant cavity between graphene and AuNPs on the pyramids, the reflected light can be absorbed again by AuNPs when the light is constantly reflected in resonant cavity, contributing to the generation of the maximum electric field enhancement. Therefore, the excellent SERS behaviors of the proposed hybrid SERS substrate can be enhanced: (1) the pyramidal structure can be employed as the amplifier for incident light and induced large electrical field intensity of the plasmonic resonance. (2) the Au plasmons will be excited again on resonant cavity between graphene and AuNPs on the pyramids.

Similar work have been studied on the electric enhancement of two dimensional material/NPs by other scholars. Zhang et al. [43] fabricated hat-shaped Ag NP/MoS₂/Au NP structures with different space curvatures SERS substrate. The electromagnetic field intensity of the 500-AgNPM-AuH is much larger than that of the flat substrate, contributing to the improving of the exciting light location. Zhang et al. [44] fabricated MoS₂/Au/Ag SERS substrate by the hydrothermal method. The “hot spots” were formed between AuNPs and AgNPs due to the LSPR effect of nanoparticles.

The roughness of micro/nanostructures is an important geometrical factor that affect the Raman signal. Nanometric surface roughness could further increase the Raman intensity. Our experimental results show that the SERS performance improved with the increase of the surface roughness. The pile-up or pyramid on the substrate surfaces with high roughness can produce more adsorption sites for target molecules.

The number of the graphene layers is influenced by the topographies. Chang et al. [45] used molecular dynamics to simulate the nano-indenter scratching process of few-layer graphene. The simulation results show that the pile-up of graphene is generated during the scraping motion of the indenter. The disorder and plastic mobility of graphene increased during nanoscratching. Fang et al. [46] studied the effect of nanoindentation on graphene by molecular dynamics simulation. As the depth of the indentation increases, the stress wave diffuses from the center, generating ripples, pile-up and wrinkles of graphene. Peng et al. [47,48] studied the load bearing capacity of Cu-graphene substrate using molecular dynamics simulation. The Cu-based graphene substrate prevents the dislocation slipping. The interaction between dislocation and graphene is the mainly strengthening mechanism.

According to the above scholars' research, the wrinkle and pile-up of graphene are generated using the nanoindentation method. The cone cavities with a larger machining parameters (Cone 1, Cone 2) are formed. The graphene do not formed the concentration of stress and the wrinkles of graphene do not stacked due to the dispersing stress. The single layer is generated on the Cu-based graphene with the larger machining parameters. In addition, the substrate surface morphology changed greatly with the smaller machining parameters (Cone 8, Cone 9). Wrinkled graphene was induced by the concentration of stress. The graphene on the pile-ups

region or the pyramid region was folded or bended through the overlap of adjacent cone cavities, resulting in the increasing number of layers of graphene.

Due to the high affinity of the probe molecule to the graphene layer, graphene is used to chemical enhancement of SERS, and the enhancement mechanism is induced by the strong chemical bond interaction between the molecule and the graphene layer. Graphene could serve as not only a protective layer for suppressing the oxidation of the Cu, but also a molecule harvester for target molecules adsorption, thereby effectively improving the performance of the SERS substrate. In addition, one graphene layer is distributed on Cone 1, Cone 2 and Cone 3 while two layers of graphene are distributed on Cone 5, Cone 7, Cone 8 and Cone 9. Other scholars show the similar conclusions. Ling et al. [49] found that the chemical enhancement of bilayer graphene was stronger than that of monolayer graphene. Monolayer and bilayer graphene have different electronic structure and then doping effect of probe molecules. The Fermi level of monolayer graphene with the low concentration of the probe molecules declined more than that of bilayer and trilayer graphene. The Fermi level of monolayer graphene with the low concentration of the probe molecule is much lower than the HOMO of the probe molecule, and the Fermi level of bilayer graphene is higher. In addition, the electron density of bilayer graphene is greater than that of monolayer graphene. The two reasons show that the SERS based on graphene intensity of bilayer graphene is greater than that of monolayer graphene at low concentration. Hao et al. [50] fabricated nanopore array microstructure by EBL lithography. Due to the CM enhancement induced by the charge transfer between graphene and probe molecules, the nanostructured substrate with graphene shows about 3 times or 9 times of MB Raman signal enhancement compared with the gold-coated nanopore or nanoparticle substrate without graphene. Therefore, in the tip-based indentation, the distribution of graphene layers onto the substrate surface is also evidently affected by the predesigned interspaces between adjacent cone cavities which increases the activity of the SERS substrates through chemical enhancement.

5. Conclusions

In this study, a hybrid substrate of the arrayed Au nanoparticle/graphene/Cu cone cavities was fabricated using conical tip-based indentation. The enhanced Raman spectrum intensity of the SERS substrate was attributed to coupled effect of the tip-based indentation-induced structural features, high surface roughness and graphene.

By varying the interspace of pre-defined cone cavities, which can be achieved by using different machining feed in tip-based indentation process, the SERS signal of hybrid substrate could be enhanced. The typical Raman peaks of Cone 9 at 652 cm⁻¹ and 1294 cm⁻¹ were chosen and the RSDs were calculated as 6.55% and 6.73%, respectively. Using the fabricated hybrid substrates, both Raman spectrum of 10⁻⁷ mol/L PQ and the 10⁻⁹ mol/L MG were successfully detected. The new hybrid SERS substrate possess excellent potential to detect agricultural residues.

Declaration of Competing Interest

The authors declare that they have no known competing financial interests or personal relationships that could have appeared to influence the work reported in this paper.

Acknowledgments

The authors acknowledges the National Natural Science Foundation of China, China (grants No. 51905047), Science and Technology Development Plan Project of Jilin Province, China (grant No.20210101388JC), the Jilin Postdoctoral Science Foundation, China and Jilin Association for Science and Technology, China (grant No. QT202022).

Appendix A. Supplementary data

Supplementary data to this article can be found online at <https://doi.org/10.1016/j.jmrt.2022.12.001>.

REFERENCES

- [1] Loganathan C, John SA. Naked eye and spectrophotometric detection of chromogenic insecticide in aquaculture using amine functionalized gold nanoparticles in the presence of major interferents. *Spectrochim Acta A* 2017;173:837–42.
- [2] Mitrowska K, Posylniak A, Zmudzki J. The effects of cooking on residues of malachite green and leucomalachite green in carp muscles. *Anal Chim Acta* 2007;586:420–5.
- [3] Dong JX, Xu C, Wang H, Xiao ZL, Gee SJ, Li ZF, et al. Enhanced sensitive immunoassay: noncompetitive phage anti-immune complex assay for the determination of malachite green and leucomalachite green. *J Agric Food Chem* 2014;62:8752–8.
- [4] Gavrilenko NA, Volgina TN, Pugachev EV, Gavrilenko MA. Visual determination of malachite green in sea fish samples. *Food Chem* 2019;274:242–5.
- [5] Ahmad AA, Ahmad MA, Yahaya NKE, Din ATM, Yaakub ARW. Honeycomb-like porous-activated carbon derived from gasification waste for malachite green adsorption: equilibrium, kinetic, thermodynamic and fixed-bed column analysis. *Desalination Water Treat* 2020;196:329–47.
- [6] Sun ZR, Yang ZZ, Wang MM, Huang CB, Ren Y, Zhang W, et al. Paraquat induces pulmonary fibrosis through Wnt/ β -catenin signaling pathway and myofibroblast differentiation. *Toxicol Lett* 2020;333:170–83.
- [7] Luo HR, Wang XH, Huang YQ, Lai KQ, Rasco BA, Fan YX. Rapid and sensitive surface-enhanced Raman spectroscopy (SERS) method combined with gold nanoparticles for determination of paraquat in apple juice. *J Sci Food Agric* 2018;98:3892–8.
- [8] Heydebreck F. Monitoring of Paraquat in soya products intended for animal feed. *Int J Food Contam* 2021;8:1–9.
- [9] Afkhami A, Moosavi R, Madrakian T. Preconcentration and spectrophotometric determination of low concentrations of malachite green and leuco-malachite green in water samples by high performance solid phase extraction using maghemite nanoparticles. *Talanta* 2010;82:785–9.
- [10] Gao Z, Li Y, Ma Y, Ji W, Chen T, Ma X, et al. Functionalized melamine sponge based on beta-cyclodextrin-graphene oxide as solid-phase extraction material for rapidly pre-enrichment of malachite green in seafood. *Microchem J* 2019;150:104167–72.
- [11] Ghavidel F, Shahtaheri SJ, Torabbeigi M, Froushani AR. Optimization of solid phase microextraction procedure for determination of paraquat using reduction process. *J Anal Chem* 2016;71:648–52.
- [12] Jia J, Yan S, Lai XX, Xu YZ, Liu T, Xiang YH. Colorimetric aptasensor for detection of malachite green in fish sample based on RNA and gold nanoparticles. *Food Anal Methods* 2018;11:1668–76.
- [13] Dong X, Chen SY, Zhou J, Wang LY, Zha LS. Self-assembly of monodisperse composite microgels with bimetallic nanorods as core and PNIPAM as shell into close-packed monolayers and SERS efficiency. *Mater Des* 2016;104:303–11.
- [14] Yan D, Qiu LL, Xue M, Meng ZH, Wang YF. A flexible surface-enhanced Raman substrates based on cellulose photonic crystal/Ag-nanoparticles composite. *Mater Des* 2019;165.
- [15] Ding SY, Yi J, Li JF, Tian ZQ. A theoretical and experimental approach to shell-isolated nanoparticle-enhanced Raman spectroscopy of single-crystal electrodes. *Surf Sci* 2015;631:73–80.
- [16] Ji C, Lu JX, Shan BJ, Li FR, Zhao XF, Yu J, et al. The origin of Mo_2C films for surface-enhanced Raman scattering analysis: electromagnetic or chemical enhancement? *J Phys Chem Lett* 2022:8864–71.
- [17] He X, Liu Y, Xue XG, Liu JH, Liu Y, Li ZB. Ultrasensitive detection of explosives via hydrophobic condensation effect on biomimetic SERS platforms. *J Mater Chem C* 2017;5:12384–92.
- [18] Sivashanmugan K, Liao JD, Liu BH, Yao CK, Luo SC. Ag nanoclusters on ZnO nanodome array as hybrid SERS-active substrate for trace detection of malachite green. *Sensor. Actuat. B-Chem.* 2015;207:430–6.
- [19] Huang T, Cao L, Zhang X, Xiong XY, Xu JJ, Xiao RS. A facile method to fabricate a novel 3D porous silicon/gold architecture for surface enhanced Raman scattering. *J Alloys Compd* 2019;790:127–33.
- [20] Wang Z, Wen X, Feng Z, Lin L, Liu R, Huang P, et al. Highly ordered Au-Ag alloy arrays with tunable morphologies for surface enhanced Raman spectroscopy. *Chem Eng J* 2018;345:389–94.
- [21] Dong SL, Wang YH, Liu ZQ, Zhang WW, Yi KZ, Zhang XA, et al. Beehive-inspired macroporous SERS probe for cancer detection through capturing and analyzing exosomes in plasma. *ACS Appl. Mater. Inter.* 2020;12:5136–46.
- [22] Zhang XA, Zhang XL, Luo CL, Liu ZQ, Chen YY, Dong SL, et al. Volume-enhanced Raman scattering detection of viruses. *Small* 2019;15:1805516.
- [23] Palermo G, Ripa M, Conti Y, Vestri A, Castagna R, Fusco G, et al. Plasmonic metasurfaces based on pyramidal nanostructures for high-efficiency SERS biosensing. *ACS Appl. Mater. Inter.* 2021;13:43715–25.
- [24] Durmanov NN, Guliev RR, Eremenko AV, Boginskaya IA, Ryzhikov IA, Trifonova EA, et al. Non-labeled selective virus detection with novel SERS-active porous silver nanofilms fabricated by Electron Beam Physical Vapor Deposition. *Sensor. Actuat. B-Chem.* 2018;257:37–47.
- [25] Bharati MSS, Soma VR. Flexible SERS substrates for hazardous materials detection: recent advances. *Opto-Electronic Advances* 2021;4:210048.
- [26] Cortijo-Campos S, Ramirez-Jimenez R, Climent-Pascual E, Aguilar-Pujol M, Jimenez-Villacorta F, Martinez L, et al. Raman amplification in the ultra-small limit of Ag nanoparticles on SiO_2 and graphene: size and inter-particle distance effects. *Mater Des* 2020;192:108702.

- [27] Zhao YD, Xie YZ, Bao ZY, Tsang YH, Xie LM, Chai Y. Enhanced SERS stability of R6G molecules with monolayer graphene. *J Phys Chem C* 2014;118:11827–32.
- [28] Zhao Y, Chu BH, Zhang LC, Zhao FZ, Yan JL, Li XY, et al. Constructing sensitive SERS substrate with a sandwich structure separated by single layer graphene. *Sensor. Actuat. B-Chem.* 2018;263:634–42.
- [29] Wu HP, Niu G, Ren W, Jiang LY, Zhao JY, Quan Y, et al. Highly sensitive label-free detection of analytes at different scales using uniform graphene-nanopyramids hybrid SERS system. *Sensor. Actuat. B-Chem.* 2022;354:131205.
- [30] Zhao X, Dong J, Cao E, Han Q, Gao W, Wang Y, et al. Plasmon-exciton coupling by hybrids between graphene and gold nanorods vertical array for sensor. *Appl Mater Today* 2019;14:166–74.
- [31] Zhang JR, Wang Y, Zhang XM, Xie WK, Li J, Wang ZB. Study of the fabrication of gold nanoparticle-graphene-arrayed micro/nanocavities as SERS substrates compared to two different angles of triangular pyramid tips. *Langmuir* 2022;38:4894–905.
- [32] Zhang JR, Yan YD, Hu ZJ, Zhao XS. Study of the control process and fabrication of microstructures using a tip-based force control system. *P. I. Mech. Eng. B-J Eng.* 2018;232:1928–42.
- [33] Li C, Hu YX, Zhang FH, Geng YQ, Meng BB. Molecular dynamics simulation of laser assisted grinding of GaN crystals. *Int J Mech Sci* 2023;239:107856.
- [34] Dong Z, Yan YD, Ge P, Li C, Geng YQ. Effects of sandwiched film thickness and cutting tool water contact angle on the processing outcomes in nanoskiving of nanowires. *Mater Design* 2023;225:111438.
- [35] Wang JQ, Yan YD, Li C, Geng YQ. Material removal mechanism and subsurface characteristics of silicon 3D nanomilling. *Int J Mech Sci* 2023;242:108020.
- [36] Peng Z, Yan Z, Sun Z, Tour JM. Direct growth of bilayer graphene on SiO₂ substrates by carbon diffusion through nickel. *ACS Nano* 2011;5:8241–7.
- [37] Chen S, Cai W, Piner RD, Suk JW, Wu Y, Ren Y, et al. Synthesis and characterization of large-area graphene and graphite films on commercial Cu-Ni alloy foils. *Nano Lett* 2011;11:3519–25.
- [38] Kumar P, Khosla R, Soni M, Deva D, Sharma SK. A highly sensitive, flexible SERS sensor for malachite green detection based on Ag decorated microstructured PDMS substrate fabricated from Taro leaf as template. *Sensor. Actuat. B-Chem.* 2017;246:477–86.
- [39] Feng L, Duan J, Wang K, Huang L, Xiao G. Efficient fabrication of highly sensitive AgNPs-drawing paper SERS substrates by robotic writing approach. *Spectroc. Acta Pt. A-Molec. Biomolec. Spectr.* 2021;261:120064.
- [40] Espinosa HD, Prorok BC, Peng B. Plasticity size effects in free-standing submicron polycrystalline FCC films subjected to pure tension. *J Mech Phys Solid* 2004;52:667–89.
- [41] Gong JL, Lipomi DJ, Deng JD, Nie ZH, Chen X, Randall NX, et al. Micro- and nanopatterning of inorganic and polymeric substrates by indentation lithography. *Nano Lett* 2010;10:2702–8.
- [42] Mao P, Liu CX, Favraud G, Chen Q, Han M, Fratolocchi A, et al. Broadband single molecule SERS detection designed by warped optical spaces. *Nat Commun* 2018;9:5428.
- [43] Zhang C, Li ZX, Qiu S, Lu WX, Shao MR, Ji C, et al. Highly ordered arrays of hat-shaped hierarchical nanostructures with different curvatures for sensitive SERS and plasmon-driven catalysis. *Nanophotonics-Berlin* 2022;11:33–44.
- [44] Zhang C, Ji C, Yu J, Li Z, Li ZX, Li CH, et al. MoS₂-based multiple surface plasmonic coupling for enhanced surface-enhanced Raman scattering and photoelectrocatalytic performance utilizing the size effect. *Opt Express* 2021;29:38768–80.
- [45] Chang WY, Fang TH, Weng CI, Yang JC. Mechanical characterizations and interface dynamics of nanoscratched graphene using molecular dynamics. *J Comput Theor Nanosci* 2013;10:832–7.
- [46] Fang TH, Wang TH, Yang JC, Hsiao YJ. Mechanical characterization of nanoindented graphene via molecular dynamics simulations. *Nanoscale Res Lett* 2011;6:481.
- [47] Peng WX, Sun K, Abdullah R, Zhang M, Chen J, Shi JQ. Strengthening mechanisms of graphene coatings on Cu film under nanoindentation: a molecular dynamics simulation. *Appl Surf Sci* 2019;487:22–31.
- [48] Peng W, Sun K, Zhang M, Shi JQ, Chen J. Effects of graphene coating on the plastic deformation of single crystal copper nano-cuboid under different nanoindentation modes. *Mater Chem Phys* 2019;225:1–7.
- [49] Ling X, Wu JX, Xie LM, Zhang J. Graphene-thickness-dependent graphene-enhanced Raman scattering. *J Phys Chem C* 2013;117:2369–76.
- [50] Hao QZ, Wang B, Bossard JA, Kiraly B, Zeng Y, Chiang IK, et al. Surface-enhanced Raman scattering study on graphene-coated metallic nanostructure substrates. *J Phys Chem C* 2012;116:7249–54.